HHS Public Access

Author manuscript

Mech Ageing Dev. Author manuscript; available in PMC 2022 June 01.

Published in final edited form as:

Mech Ageing Dev. 2021 June ; 196: 111471. doi:10.1016/j.mad.2021.111471.

Evolving Structure-Function Relations during Aortic Maturation and Aging Revealed by Multiphoton Microscopy

Cristina Cavinato[1], **Sae-Il Murtada**[1], **Alexia Rojas**[1], **Jay D. Humphrey**[1,2]

[1]Department of Biomedical Engineering Yale University, New Haven, CT, USA

[2]Vascular Biology and Therapeutics Program Yale School of Medicine, New Haven, CT, USA

Abstract

The evolving microstructure and mechanical properties that promote homeostasis in the aorta are fundamental to age-specific adaptations and disease progression. We combine *ex vivo* multiphoton microscopy and biaxial biomechanical phenotyping to quantify and correlate layer-specific microstructural parameters, for the primary extracellular matrix components (fibrillar collagen and elastic lamellae) and cells (endothelial, smooth muscle, and adventitial), with mechanical properties of the mouse aorta from weaning through natural aging up to one year. The aging endothelium was characterized by progressive reductions in cell density and altered cellular orientation. The media similarly showed a progressive decrease in smooth muscle cell density and alignment though with inter-lamellar widening from intermediate to older ages, suggesting cell hypertrophy, matrix accumulation, or both. Despite not changing in tissue thickness, the aging adventitia exhibited a marked thickening and straightening of collagen fiber bundles and reduction in cell density, suggestive of age-related remodeling not growth. Multiple microstructural changes correlated with age-related increases in circumferential and axial material stiffness, among other mechanical metrics. Because of the importance of aging as a risk factor for cardiovascular diseases, understanding the normal progression of structural and functional changes is essential when evaluating superimposed disease-related changes as a function of the age of onset.

Keywords

mouse; homeostasis; natural aging; layer-specific microstructure; biaxial mechanics

1. Introduction[1]

The aorta plays a central role in overall cardiovascular function. Its primary mechanical function is to store elastic energy when deforming during systole and to use this energy to

Address for Correspondence: J.D. Humphrey, Ph.D., Department of Biomedical Engineering, Malone Engineering Center, Yale University, New Haven, CT 06520 USA, jay.humphrey@yale.edu, +1-203-432-6528.

[1]DTA (descending thoracic aorta), ECM (extracellular matrix), EC (endothelial cell), SMC (smooth muscle cell), FB (fibroblast), SHG (second harmonic generation), 3D (three-dimensional)

work on the blood during diastole to augment flow (Wagenseil and Mecham, 2009) while ensuring sufficient mechanical strength to protect against structural failure in response to hemodynamic loads (Humphrey and Tellides, 2019). These unique characteristics arise from the multi-layered composite structure of the wall, with two extracellular matrix (ECM) components dominating the passive mechanical behavior: elastic fibers, consisting of an elastin core and elastin-associated glycoproteins, which contribute to aortic compliance and resilience, and fibrillar collagens, mainly types I and III but also associated collagen V, small leucine-rich proteoglycans, and matricellular proteins, which together endow the wall with significant stiffness and strength.

The microstructure of the aorta and its associated mechanical properties and structural integrity are regulated by three primary cell types. Endothelial cells (ECs) sense diverse stimuli, especially the shear stress induced by blood flow but also circumferential and axial stresses/stretches induced by blood pressure and motion (Baeyens et al., 2016). Smooth muscle cells (SMCs) serve as central nodes in establishing, maintaining, remodeling, and repairing the medial layer in response to mechanical stimuli (Fisher, 2010). Fibroblasts (FBs) exhibit a similar ECM regulatory function in the adventitia, though likely augmented by resident macrophages (Majesky, 2015). All three of the primary cell types function in large part via mechanosensing (assessment) of their local mechanical environment, with SMCs and FBs responsible for continued mechanoregulation of ECM (deposition, remodeling, and removal) to promote mechanical homeostasis (Humphrey et al., 2014). Cell numbers and phenotype vary during maturation and aging, with aging a strong independent risk factor for many cardiovascular diseases (Greenwald, 2007).

Notwithstanding the value of traditional analyses of the global properties of the wall, such as pulse wave velocity, each aortic region exhibits different local characteristics (Roccabianca et al., 2014; Bersi et al., 2017). Moreover, the descending thoracic aorta (DTA) is unique compared to other elastic arteries since its dorsal side is affixed to the spine through adipose tissue and intercostal branches. Two-photon imaging is a nondestructive method suitable for *ex vivo* assessment of regional microstructural properties of aortic wall components in loaded conditions, whether combined with biomechanical testing or not (Haskett et al., 2012; Tsamis et al., 2013; Krasny et al., 2018; Yu et al., 2018; Cavinato et al., 2020). This approach is especially useful in model organisms such as mice due to the thinness of the aortic wall, which allows observations with minimal limitations of optical penetration. Prior studies using this technique for studying murine arteries under *in vivo* equivalent conditions yet remain limited and mainly focused on one constituent at a time (e.g., Wan et al., 2012; Haskett et al., 2012; Spronck et al., 2016; Yu et al., 2018). As a result, there are few reports wherein results are compared for multiple constituents, particularly across maturation and aging at age-specific multiaxial loading conditions despite the importance of understanding effects of aging (Wan and Gleason, 2013). Although mice are commonly used to study aging-related vascular disease (e.g., Fleenor et al., 2010; Donato et al., 2013; Ferruzzi et al., 2018), it is important to note that relationships between murine and human aging are nonlinear, with mice having a shorter and much accelerated early phase than humans (Dutta and Sengupta, 2016). The interested reader is also referred to available rich databases (Flurkey et al., 2007; Geifman and Rubin, 2013).

In this paper, we combine three-channel multiphoton microscopy and computer-controlled biaxial testing to quantify aortic microstructure and properties in normal mice as a function of postnatal maturation and natural aging up to one year. Toward this end, we introduce a new approach to quantify multiple structural parameters for the primary extracellular components–collagen and elastic lamellae–and three fundamental cell types – ECs, SMCs, adventitial cells – locally, in 3D, and as a function of biaxial loading.

2. Materials and Methods

2.1. Sample preparation and biaxial testing

All animal protocols were approved by the Institutional Animal Care and Use Committee of Yale University. Segments of DTA were collected from 20 female C57BL/6J mice at postnatal ages of P21 days (n=4), P42 (n=4), P98 (n=4), P230 (n=4), and P365 (n=4) following euthanasia by an intraperitoneal injection of Beuthanasia-D (150 mg/kg) and exsanguination. The aorta was flushed of blood with a Hanks buffered saline solution (HBSS), then the DTA was isolated, cleaned, excised between the first and the fourth pair of intercostal branches, and prepared for mechanical testing as before (Ferruzzi et al., 2013). Briefly, samples were secured on glass cannulae with 6-0 sutures, then immersed in HBSS at room temperature (which reduces SMC contractility) within a custom computer-controlled biaxial testing device (Gleason et al., 2004). Following passive preconditioning via four distension cycles from 10 mmHg to an age-specific maximum luminal pressure (100 mmHg for P21, 120 mmHg for P42, and 140 mmHg for P98, P230, and P365), while maintained at the age-specific *in vivo* axial stretch, seven passive distension-extension testing protocols were: three cycles of pressure-diameter testing between 10 mmHg and the age-specific maximum pressure at three different fixed values of axial stretch corresponding to the *in vivo* value and ± 5% of this value, then four cycles of axial force-length testing between a load of 0 g to the maximum load reached at the maximum pressure and *in vivo* +5% axial stretch at a fixed luminal pressure of 10, 40, 70, and 100 mmHg for P21, or 10, 40, 80, and 120 mmHg for P42 samples, or 10, 60, 100, and 140 mmHg for P98, P230 and P365 samples (following the age-specific protocol in Murtada et al. (2020)). Experience has shown that data from these seven protocols enable robust fixed-point estimates of constitutive parameters via nonlinear regression (Ferruzzi et al., 2013). Toward this end, values of luminal pressure, axial force, outer diameter, and axial length were recorded throughout testing (Figure 1a).

Mechanical data analysis also followed prior reports (Ferruzzi et al., 2013), whereby radially averaged (mean) values of stretch and stress were computed as: circumferential (θ) and axial (z) components of the left (and right, in the absence of rigid body rotations) stretch tensor $\lambda_\theta = (od - h)/(OD - H)$ and $\lambda_z = \ell/L$, and circumferential and axial components of the Cauchy stress tensor as $\sigma_\theta = Pa/h$ and $\sigma_z = (f_z + P\pi a^2)/\pi h(2a + h)$. In order, od and OD denote the loaded and unloaded outer diameter, h and H the loaded and unloaded thickness, ℓ and L the loaded and unloaded axial length, P the transmural pressure, a the loaded luminal radius, and f_z the measured axial force. The energetically preferred value of axial stretch λ_z is referred to as the *in vivo* value and is inferred as that value at which axial force does not change during cyclic pressurization (see Figure 2 in Ferruzzi et al. (2013) for a detailed

description of this and other sample-specific biomechanical parameters). Biomechanical metrics that characterize the nonlinear passive mechanical behavior of the DTAs include the mean circumferential and axial stress, circumferential and axial material stiffness, and the elastically stored energy, which is determined from data during unloading because dissipated energy associated with hysteresis is not available to work on the contained fluid. These key metrics are calculated using best-fit values of eight parameters within a so-called four-fiber family model, which in terms of stored energy function is:

$$W = \frac{c}{2}(\mathrm{I}_1 - 3) + \sum_{\mathrm{i}=1}^{4} \frac{c_1^i}{4c_2^i}\{\exp[c_2^i(\mathrm{I}_4^i - 1)^2)] - 1\}, \quad (1)$$

where c, c_1^1, c_2^1, c_1^2, c_2^2, $c_1^{3,4}$, $c_2^{3,4}$ are material parameters, I_1 is the first invariant of the right Cauchy-Green tensor, and $\mathrm{I}_4^{\mathrm{i}} = \lambda_\theta^2 \sin^2 \alpha_0^{\mathrm{i}} + \lambda_z^2 \cos^2 \alpha_0^{\mathrm{i}}$ with α_0^{i} the fiber angle with respect to the axial direction in the intact traction-free configuration. We let $\alpha_0^1 = 0$ (axial) and $\alpha_0^2 = \pi / 2$ (circumferential) but estimate $\alpha_0^{3,4} = \pm \alpha_0$ (symmetric diagonal) as part of the nonlinear regression, which minimizes the sum-of-the-squared differences between theoretical and experimental values of normalized luminal pressure and axial force (Ferruzzi et al., 2013). These “four fiber families” need not represent actual orientations; rather, they capture phenomenologically all contributions to the mechanical behavior including those due to cross-links, physical entanglements, and other microstructural complexities not easily quantified. Indeed, the circumferential family captures contributions by both circumferentially oriented collagen and passive smooth muscle in the media, which cannot be distinguished during bulk testing. The overall utility of this relation has been verified independently to describe biaxial data well (Schroeder et al., 2018).

Another parameter describing the passive mechanical behavior, and often used clinically to evaluate structural stiffness, is the distensibility:

$$D = \frac{od_{sys} - od_{dias}}{od_{dias}(P_{sys} - P_{dias})}, \quad (2)$$

where *sys* and *dias* denote systolic and diastolic and the relative blood pressures P_{sys} and P_{dias} were measured using the tail-cuff technique in conscious mice under resting conditions.

Following biaxial mechanical testing, the specimen was removed from the device and re-cannulated on a custom blunt-ended triple-needle assembly with the proximal end secured to a fixed needle and the distal end to a sliding one (Bersi et al., 2016). This needle assembly allowed pressurization, recorded by a digital manometer, and variation of axial stretch by controlling the free-end of the needle with a micrometer while keeping the sample in a stable configuration for two-photon imaging while immersed in HBSS at room temperature. This design (Figure 1b) enabled the co-axial needle to be rotated about the long axis of the vessel, thus presenting different sides (ventral and dorsal) of the aorta to the objective of a multiphoton microscope. Prior to imaging, cell nuclei within the sample were stained by incubation in a 2 μM red fluorescent nucleic acid stain (SYTO™) solution for 2 hours.

2.2. Two-photon microscopy

A two-photon microscope, with a Titanium-Sapphire Laser (Chameleon Vision II, Coherent), was used to delineate simultaneously three components of the aortic wall: fibrillar collagens, elastic fibers, and cell nuclei. The microscope was equipped with a water immersion 20X objective lens (N.A. 0.95) and tuned at a wavelength of 840 nm. The second harmonic generation (SHG) signal arising from collagen structures was detected in the wavelength range of 390-425 nm. The two-photon auto-fluorescent signal of elastin structures was collected in the range of 500-550 nm. The fluorescent signal of cell nuclei was detected in a wavelength range higher than 550 nm. The laser power was set to prevent saturation of any of the three signals. Three-dimensional (3D) images were acquired with an in-plane field of view (axial-circumferential plane of the DTA) of 500 μm x 500 μm and a volume of about 0.05 mm^3. Numerical imaging resolution was 0.48 μm/pixel, while the out-of-plane (radial axis of the sample) step size was 1 μm/pixel.

Before image acquisition, the microscope objective was centered over a specific region and the needle assembly was rotated to present a particular surface, first dorsal then ventral. The former was localized relative to the position of the intercostal branches, with image acquisitions at an equidistant position between the same two pairs of branches. Samples were tested at three different *ex vivo* equivalent blood pressures: systolic, diastolic, and half-diastolic. The systolic pressure was, respectively, 90 mmHg and 114 mmHg for P21 and P42, and 127 mmHg for P98, P230 and P365 mice; the diastolic pressure was 50 mmHg for P21 and 80 mmHg for P42, P98, P230 and P365 mice. These values were chosen as average values of *in vivo* measurements at comparable ages (Wagenseil and Mecham, 2009; Hawes et al., 2020; Murtada et al., 2020). After preconditioning again, with four pressurization cycles between zero and systolic pressure, the pressure was first fixed at half-diastolic and 3D images of the aortic wall were acquired at sample-specific *in vivo* axial stretch determined by the biaxial mechanical testing. Images were similarly acquired at diastolic, then systolic pressures. A 180-degree rotation around the axis of the needle allowed imaging of the ventral region, with images acquired again. Finally, the length of the sample was adjusted to a stretch 5% less than *in vivo* then 5% greater than *in vivo*. The sample was checked for radial movement due to leaks or relaxation during a pressure stabilization period before each acquisition.

2.3. Two-photon image analysis

Each image for the three signals (collagen, elastin, and nuclei) was post-processed using MATLAB R2019b and ImageJ 1.53a. Due to the near cylindrical shape of the DTA samples, analysis of separate layers of the wall would be difficult using the source images because the structural layers (medial and adventitial, and similarly individual medial lamellae) are not located on parallel planes. To simplify the analysis, a custom MATLAB algorithm performed pixel-by-pixel cross-sectional slicing of 3D images in the circumferential-radial plane to fit a circle onto the two-dimensional mid-thickness profile of the wall of each slide, to use the mean center coordinates of the circles to transform each circumferential-radial slice from Cartesian to polar coordinates (angle and radius), and to store the resulting 3D images with the new coordinates (Figure 1c). Image distortions due to the coordinate transformation appeared negligible after careful comparisons of images before and after

transformation and because the inner diameter of the samples was at least five times the radial distance. The transformed 3D images were used for the microstructural analysis of the three components through the parameters described here below.

Layer-specific thickness and volume fraction—Layer-specific thickness was defined by acquiring mean intensity profiles of multiple volume subunits (25 measurements uniformly distributed across the axial-circumferential plane) along the radial axis of each transformed 3D image for the three different signals (Supplemental Figure S1a). The internal and external limits for each of the three components were defined automatically by selecting radial positions beyond which the area under the two tails of the normalized intensity profile corresponded to defined thresholds. These thresholds were set using a training set of ten 3D images selected from all acquired images (two images per age group, one at the highest pressure and stretch configuration and one at the lowest), where the internal and external limits for each component were selected manually. The boundaries of the wall were identified as the limit for cell (EC) nuclei and adventitial collagen, respectively. The interface between the medial and adventitial layers was identified as a function of a characteristic tightening of the slope of the mean intensity profile for cell nuclei along the radial direction; this behavior of the nucleus radial intensity corresponds in all images to the emergence of the outer layer of smooth muscle cells of the media. The interface between adventitia and media was thus defined automatically as a function of the radial position of the maximum derivative increment of the intensity profile of the nuclei signal within the radial range between the position of the peak of the collagen intensity profile and the inner surface of the aorta, following confirmation with the set of training images (see Video S2 for an example).

Each 3D image was then binarized using constant thresholds specific for each signal. Thresholds were previously defined on the same training set using the Otsu method, which allowed segmentation from the background and contour preservation of collagen fibers, elastic lamellae, and nuclei in all directions. Intensity profiles were acquired after binarization for the same volume subunits used for thickness analysis (25, uniformly distributed on the axial-circumferential plane). Component volume fractions (VFs) related to the adventitia and media were defined as a black:white pixel ratio between the specific limits of each layer measured previously for each volume subunit. The volume fractions were the average of the subunit's values of each 3D image (Figure S1b). Note that this total volume was a relative sum of fibrillar collagen, elastin, and nuclei, which does not consider other components (e.g., cytoplasm, non-fibrillar collagen, and GAGs). A pilot analysis of the radial intensity profile for the thickest samples revealed that the murine aorta induced a minimal signal decay due to light penetration, thus confirming robustness of the method (Figure S2).

Collagen fibers: straightness, alignment, bundle width—The in-plane (i.e., axial-circumferential plane) straightness, or alternatively the reciprocal of the in-plane waviness, of the collagen fibers was measured using ImageJ line drawing functions. The straightness of a collagen fiber k was computed as the ratio of the end-to-end (L_o) to the total (L_f) fiber length (Figure 1d):

$$P_s^k = \frac{L_o^k}{L_f^k} \,. \tag{3}$$

An algorithm was developed to automatically select restricted positions in the 3D image defined consistently at a uniform distance and at different depths through the layer-specific thicknesses of each 3D image. For each position (n=25), the closest collagen fiber was selected for the straightness measurement. The collagen fiber bundle next to each previously selected fiber was then selected and its width (i.e., the transversal section in the axial-circumferential plane) determined.

The in-plane alignment of the collagen fibers was determined by measuring the concentration of in-plane orientations around a primary orientation. Alignment related to the out-of-plane component was minimal similar to previous studies (Schriefl et al., 2012; Cavinato et al., 2017), thus reducing the analysis to a planar axial-circumferential problem. The in-plane distribution of orientation was estimated for each circumferential-axial image using a 2D structure tensor analysis, namely OrientationJ plug-in for ImageJ (Rezakhaniha et al., 2012). The resulting orientation histograms, after averaging along the radial direction and normalizing by the area under the mean distribution, revealed a primary orientation in the axial direction determined primarily by the dominant contribution of the adventitial collagen. The mean orientation distribution of each 3D image was nevertheless parameterized with the Von Mises circular probability density function (as a function θ; Figure S1c):

$$\mathrm{F}(\theta \mid \mu, \kappa) = \frac{1}{2\pi I_0(\kappa)} e^{\kappa \cos(\theta - \mu)} \tag{4}$$

where μ is the primary orientation, I_0 is the modified Bessel function, and κ is the alignment parameter, a measure of concentration that quantifies collagen fiber alignment at the tissue level; it differs in scale from a measure of fiber straightness, which is at the level of single collagen fibers. Finally, collagen bundles were evaluated simultaneously with the in-plane straightness. Noting that the majority of aortic collagen is located within the adventitia in the mouse, most collagen-specific metrics reported herein primarily reflect adventitial structure, which is appropriate for constitutive modeling given that mechanical contributions of the circumferential collagen of the media cannot be distinguished from those of the passive smooth muscle.

Cell density and cell alignment—Cell density was calculated as the number of cells per layer-specific unit volume by counting the number of nuclei in a defined volume of the 3D image and using the layer-specific thickness (Figure 1e). Three cell groups were considered based on characteristic shapes of their nuclei and radial position in the wall, namely, ECs (monolayer on intima), SMCs (in the media), and cells within the adventitia (mainly FBs). A semi-automatic algorithm selected multiple subunits of volume (100 μm x 100 μm x local layer-specific thickness, n=25) for each 3D image, with conversion to binary form by filtering and thresholding. The medial and adventitial cell numbers were then normalized by

a volume of 0.001 mm^3 to allow consistent comparisons. EC density was computed as number of cells per surface area and normalized by an area of 0.01 mm^2. Finally, the in-plane alignment of the SMCs was measured relative to the primary orientation using the same algorithm for the in-plane collagen fibers (Figure S1d).

Elastic lamellae and inter-lamellar distance—The number of, and separation distance between, elastic lamellae were measured via cross-sectional slicing of the 3D images in the circumferential-radial plane (Figure 1f). The distance between two adjacent elastic lamellae was measured by tracing five separate radial distances with ImageJ at equal steps along the axial direction of 100 μm. Lamellae thickness was extrapolated using the previous measurements and value of the medial thickness for the specific region. The thickness of the elastic lamellae, expected to be on the order of a few microns, were not recorded because they are close to the limits of lateral resolution.

2.4. Standard histology

Following mechanical testing and multiphoton imaging, the aortas were unloaded and fixed overnight in a 10% neutral buffered formalin solution, then stored in 70% EtOH at 4°C. Vessels were then embedded in paraffin, sectioned serially, and stained with Picro-Sirus Red (PSR) or Verhoeff Van Giesen (VVG). Cross-sections were imaged using an Olympus BX/51 microscope at 40x magnification (CellSens Dimension). The PSR-stained cross-sections reveal fibrillar collagen colorimetrically, with thick (orange-red) versus thin (yellow-green) fibers evident when viewed using polarized light; the VVG-stained sections reveal elastic lamellar structures in black (Figure S2).

2.5. Statistical analysis

Potential statistical differences in microstructural parameters among age groups (n=4 per group, where each value was the average of dorsal and ventral values) were assessed using a non-parametric Kruskal Wallis test followed by Dunn's multiple comparison test. Comparative statistics between dorsal and ventral regions and between pressure and axial stretch configurations (n=4 per group, with paired measures) was assessed with a non-parametric Friedman test followed by Dunn's multiple comparison test. Correlation statistics between microstructural parameters and the reported mechanical metrics (n=20, where each microstructural value was the average of dorsal and ventral values) were assessed using Pearson correlation coefficient or nonparametric Spearman correlation coefficient (normal distribution not accepted for at least one variable). Normality was checked via a Shapiro-Wilk normality test. For all reported comparisons, $p<0.05$ was considered significant, with one-to-three asterisks denoting p values lower that 0.05, 0.01 and 0.001, respectively.

3. Results

Overall, the aortic wall thinned slightly between P21 and P42, followed by a gradual and almost linear thickening to a maximum at P365 (Figure S3). Several microstructural changes accompanied these changes in wall thickness during late stages of maturation (P21-P98) and aging in adulthood (P98-P365), which can be appreciated visually (Figure 2, illustrative results) though better quantified (Figure 3, representative results) and considered

longitudinally (Figure 4, mean ± SEM), all at *ex vivo* equivalent age-specific physiologic conditions. In the following sections, layer-specific (mainly medial and adventitial; Figure S4) changes in microstructure are also quantified regionally as ventral versus dorsal (Figure S5). Because mechanical properties undergo important changes over the age range considered (Figure 5), we sought possible correlations between microstructural and mechanical parameters at comparable *ex vivo* equivalent age-specific physiologic conditions (Figures 6 and 7).

Layer-specific changes in microstructure during maturation and aging

There was a significant reduction in the density of the axially oriented EC nuclei between P21-P98 (Figure 2a, Figure 4d), with a gradual lessening of their axial orientation during aging (Figure 3b). In the media, the SMC nuclei were interposed between the elastic lamellae, occupying most of the space not occupied by the elastic structures and sparse collagen bundles (Supplemental Video S1). The elongated spiral-shaped SMC nuclei oriented primarily along the circumferential direction (Figure 2c), though local groups of cells followed marginally diagonal orientations in the circumferential-axial plane, likely alternating in sequential layers creating a slight herringbone effect at all ages. No clear out-of-plane orientation of SMC nuclei was observed in the loaded configurations for any ages. Importantly, the SMCs underwent a significant monotonic decline in density over time with the highest rate between P21-P42 (Figure 4a), and continuous relative decrease in nucleus volume fraction resulting in an associated increase in elastin volume fraction in the media (Figure 4c) despite no new deposition. SMC alignment about the primary circumferential orientation also decreased with age until stabilizing between P230 and P365 (Figure S3k).

Elastic lamellae presented as multiple locally flat sheets (Figure 2b), though with qualitatively heterogeneous thicknesses. There was no apparent difference in their planarity across ages, though a pseudo-increase in number between P21 and P365, ranging between 4-5 apparent lamellae at P21 and 5-6 at P365, suggestive of a possible fraying with aging in the absence of *de novo* production. The internal organization of these lamellae appeared heterogeneous upon circumferential-axial sectioning, consisting mainly of dense regions with multiple elastic fibers arranged individually, with a thickness of the order of 1 μm and mostly a circumferential orientation. Less dense regions were interposed within the main structure, which took on large oval shapes, elongated in the circumferential direction, within which thicker circumferentially oriented elastic fibers were arranged more irregularly. A component of these thicker elastic structures was distinguished in the radial direction, independent of age, but the analysis was limited by the out-of-plane resolution of the imaging technique. Overall, the inter-lamellar distance reduced between P21-P42, followed by an increase until P365, suggestive of increased intra-lamellar content with aging (Figure 4b).

Naturally evident medial collagen, noting that its observation has long been limited in mice via a SHG signal (Stoller et al., 2002; Sugita and Matsumoto, 2017), concentrated at the interface with the adventitia. It generally increased in volume between P21 and P98 but decreased from P98 to P365. This collagen appeared to be oriented primarily axially, similar to the adventitial collagen, for all groups except P21 (Figure 3c,d). In P21 samples, collagen

fibers closer to the lumen aligned more circumferentially but transitioned towards an axial direction farther from the lumen, thus aligning with the adventitial collagen fibers. Because the SHG signal yielding this distribution was dominated by the thicker collagen bundles located mostly in the outer layers, and because the associated elastic lamellae had undulating radial locations along the axial direction, this finding arose in part because the outer collagen bundles were less thick in P21 samples, as described below. Indeed, when observing small local medial regions not including large collagen bundles (Figure 3f), achieved via a significant increase in contrast and brightness compared to that used to visualize adventitial regions (Figures 3e and S4), thin collagen fibers with circumferential orientation but no bundle organization were evident in P21 samples. Fibers of similar appearance were also observed in older samples, though the partial presence of large bundles of collagen fibers in the medial layers and their widening with age precluded automatic capture of the circumferential component of these thin and less bright fibers in the orientation distribution for the entire layer.

The adventitial fraction of wall thickness increased slightly from P21 to P42, followed by a slight long-term decrease until P365, though not significant (Figure S3d). Collagen fiber bundles appeared to thicken and increase in volume with age, and fibers within these bundles tended to straighten gradually with a marked 3D undulation in P21 samples that was not visible in P365 samples (Figure 2d). Collagen fiber straightness increased particularly between P21 and P42, then less so with age (Figure 4g). The effect of maturation was evident for the width of the collagen bundles, with the largest increase between P21 and P42, followed by a gradual stabilization between P98 and P365 (Figure 4h). Adventitial collagen fiber angles distributed primarily about the axial direction in all age groups with a negligible radial contribution. Collagen volume fractions in the adventitia increased monotonically with aging while the volume fraction of other components decreased relatively (Figure 4f). Alignment around the primary orientation of the collagen fibers initially reduced from P21 to P42 days, then increased but reduced slightly after P98, though without statistical significance (Figure 4i). The number of adventitia cells per volume reduced between P21 and P42, with a plateau between P42 and P98 and a further decrease after P98 (Figure 4e). These characteristics were strongly influenced by the mechanical loading state, as noted further below.

Differences in collagen microstructure were observed when comparing ventral and dorsal regions for the different age groups when observed near physiological loading conditions (Figure S5). In particular, collagen straightness and alignment along the axial direction were both generally higher in the dorsal compared to the ventral region with significant differences for some ages (Figure S5e,g), suggesting more diagonally orientated and undulated collagen fibers in the ventral region. In addition, lower values, though not significantly so, of wall thickness and adventitial thickness fraction were observed in the ventral region compared to the dorsal region for all ages (Figure S5a,d). Figure S6 compares the loaded thickness measured at defined loading conditions and the average unloaded thickness measured from a ring section of the sample after the test. Linear relationships arose separately for the dorsal and ventral regions, and underlined that the ventral region was in general thinner than the dorsal region at every analyzed load condition. Other microstructural parameters did not show any consistent regional difference over all age

groups and the effects of age previously observed on the average parameters (Figure 4, Figure S3) were generally similar when considering ventral and dorsal regions separately. With the exception of the orientation distribution of collagen fibers and cell nuclei previously outlined, the microstructural parameters did not manifest any other distinctive variations along the radial direction of the wall that could be associated with age, loading conditions, or region.

Changes in microstructure due to mechanical loading

The microstructural parameters were analyzed further at *ex vivo* equivalent age-specific diastolic and systolic pressures (Figure 4) and extended to three different *ex vivo* equivalent age-specific blood pressures and three sample-specific axial stretches (Figure S7) to highlight load-dependent variations, notably for the parameters related to collagen fibers. Fiber straightness increased significantly with increases in pressure and axial stretch, appearing to reach its maximum between diastolic and systolic pressure (Figure 4g, Figure S7e). Trends in each age group suggested that the fibers became less responsive in terms of straightening with increasing age since the fibers started from a less undulated state in the configuration of lowest load. Additionally, the width of the collagen bundles decreased with increasing pressure and axial stretch, with similar behaviors across ages (Figure 4h, Figure S7f). Results at P230 and P365 represent an exception, however, with collagen bundle width remaining relatively high when axial stretch changed, though with limited changes compared to other ages. While straightness and bundle width at different loading conditions generally followed the trends with age described previously, collagen alignment was strongly influenced by the loading state and reflected two phenomena: decreased alignment (i.e., reorientation of fibers toward a more diagonal organization) with increased pressure at *in vivo* axial stretch (Figure 4i, Figure S7g) and increased alignment with increased axial stretch at diastolic pressure (Figure S7g). Changes in other microstructural parameters due to loading are also in Figure S7.

Correlating microstructure and mechanical properties during maturation and aging

Multiple morphological and mechanical metrics also showed a clear evolution as a function of age (Figure 5). In general, the most dramatic changes in mechanical parameters were observed between P21 and P98 in both axial and circumferential directions, with a stabilization or minor reversal of trends from P98 to P365. Note, too, the high sensitivity of the stored energy and stiffness parameters to physiologic pressure variations from diastolic to systolic (Figure 5c,d,f). These findings were compared versus microstructural features, revealed by an unbiased correlation matrix for the multiple sample-specific variables of interest. The loaded metrics used in the correlation analysis correspond to the age-specific *in vivo* axial stretch and either systolic or diastolic *ex vivo* equivalent pressure (Figure 6). Relationships between microstructure and other metrics that showed high correlation, at physiologic pressures, are highlighted in Figure 7.

Strong positive correlations were found between both collagen straightness and bundle width and unloaded/loaded diameter and unloaded thickness (measured with a dissection microscope after testing), suggesting consistent relationships between thicker and less undulated collagen fibers and wall growth (Figure 7d). There was also a strong negative

correlation between cell density (all types) and SMC alignment with unloaded/loaded diameter and unloaded thickness (Figure 7a). Larger diameter and wall thickness correlated with higher percentages of adventitial collagen and higher inter-lamellar space.

Significant positive correlations were also seen between collagen straightness and bundle width and both circumferential and axial stretch and stress. Circumferential stiffness correlated strongly and positively with collagen straightness and bundle width (Figure 7e), and correlated negatively with the collagen fiber alignment toward the axial direction. Moreover, cell densities correlated significantly and negatively with passive mechanical metrics in the circumferential direction of the aortic tissue. Among those, EC density decreased with increasing circumferential stiffness (Figure 7b). While at the diastolic state, medial collagen fraction correlated strongly with axial stiffness (Figure 7c), at the systolic state, this relationship gave away to a higher correlation between adventitial collagen fraction and both circumferential and axial stiffness (Figure 7f). In addition, there was a positive correlation between axial stiffness and collagen bundle estimated at systole, but not diastole.

4. Discussion

Maturation and aging of arteries are complex processes both microstructurally and mechanically. Mean arterial blood pressure and flow increase rapidly in the early postnatal period, during which time aortic composition evolves, the wall thickens, and diameter and length increase (Huang et al., 2006; Wan and Gleason, 2013). Aging further increases the diameter and wall thickness associated with additional compositional changes (Wheeler et al., 2015). Several studies report quantitative changes in primary ECM constituents, including mass or area fractions, and structural parameters associated with changes in biomechanical function at different degrees of maturation (Le et al., 2015; Murtada et al., 2020) and aging (Ferruzzi et al., 2018; Hawes et al., 2020) of murine arteries. As shown in these studies, rich descriptions of compositional change can be obtained by standard histology and immunochemistry. Nonetheless, such studies represent but a single static configuration (often unloaded during fixation) and rely on fixed samples that are dehydrated, embedded, and sectioned. Many have called for complementary imaging methods that provide microstructural information under changing physiological loading of an intact sample (Goth et al., 2016; Disney et al., 2018; Turcotte and Zhang, 2020). Multiphoton microscopy is well-suited for microstructural analysis given its non-destructive nature and 3D capability, that is, information on both composition and architecture. Multiple studies have used this technique for larger animals (Timmins et al., 2010; Schriefl et al., 2012; Tsamis et al., 2013; Chow et al., 2014; Cavinato et al., 2020), but a thick wall can limit image analysis in these cases. The mouse aorta, on the other hand, allows imaging through the entire aortic wall in most physiological and many pathological conditions with minor constraints on optical penetration without the need for clearing. Yet, multiphoton-based studies of murine arteries have remained limited, sometimes focusing on one constituent at a time (Haskett et al., 2012; Yu et al., 2018) and generally not focusing on maturation or aging, with one notable exception that considered a narrow range of aging (Wan and Gleason, 2013). Quantifying the normal maturation and aging processes was thus considered important using a consistent approach, augmented here with custom biaxial biomechanical

testing. Since distinct stages of aging occur at different rates in mice than in humans (Flurkey et al., 2007), a sufficient number of relevant age levels was required – we selected five particular ages based on aforementioned reports.

As expected, the layer-specific composition of the aortic wall varied greatly during maturation and aging. There is a near linear increase in total wall thickness under comparable *ex vivo* equivalent physiologic loading conditions with aging, starting from P42, though not due to any significant increase in the thickness of a particular layer (Figure S3a,d). By contrast, the reduction in medial layer thickness from P21 to P42 reflects different changes during maturation. Compositional changes tend to favor a higher ratio of collagen in the adventitia and elastin in the media, with medial collagen yet increasing up to P98 but gradually decreasing thereafter. These results describe a loaded configuration reflecting the *in vivo* state and thus cannot be directly compared with classic results from histological sections of unloaded samples. Nonetheless, standard histology reveals that the percent of the wall that is adventitia increases from P21 to P98, consistent with continued deposition of collagen in the adventitia between P21 and P60 (Le et al., 2015; Murtada et al., 2020). These authors also reported an increase in medial collagen with respect to the whole wall in maturation, reaching a peak at P42, consistent with our observations of the medial layer. At more advanced ages, from 6 months to 2 years, there has been a report of a gradual increase in collagen with relatively unchanged elastin content (Hawes et al., 2020).

Some of our microstructural metrics refer to collagen fibers at the tissue level, in terms of primary in-plane orientation and alignment, others at the fiber level, in terms of straightness of single fibers. Such analysis is uncommon in classical histology of murine samples. A few studies observed collagen fibers with SHG, finding mainly axial orientations in murine carotids (Wan et al., 2012; Wan and Gleason, 2013) but axial alignment shifting more toward circumferential upon pressurization in murine aortas (Haskett et al., 2012, 2013). To our knowledge, however, only one prior study evaluated collagen microstructure at multiple ages, namely in carotids at P31 and P56 in WT and *Fbln5*$^{-/-}$ mice (Wan and Gleason, 2013). There was, however, no prior assessment of alignment or straightness as a function of aging. Our findings thus extend understanding of collagen fiber structure from weaning through natural aging, demonstrating clear changes. Most notable was thickening of collagen bundles, with a gradual stabilization after P98.

Elastic lamellae were recently analyzed in detail with multi-photon microscopy, namely unfolding and stretching as a function of axial stretch and pressure in carotid arteries of P56 mice (Yu et al., 2018). Our results for inter-lamellar distances at comparable loading conditions and ages agree well with this study. By starting from loads lower than physiological, they quantified a gradient of unfolding through the thickness of the carotid that appears to equalize lamellar extension through the wall with increasing loading. Although such measurements would be interesting across maturation and aging, our quantifications focused on the physiological range, wherein the lamellae are already in an unfolded state. Prior theoretical studies have shown the utility of using *in vivo* configurations as references for stress analysis (Bellini et al., 2014). From our analysis over the first year of murine life, the elastic lamellae appeared to remain similar in appearance and number. A gradual increase in inter-lamellar distance from P42, after first decreasing

some, combined with observations by others (Hemmeryckx et al., 2013) and our results on cell density and alignment, may or may not be due in part to gradual SMC hypertrophy, but likely matrix accumulation, including glycosaminoglycans (Ferruzzi et al., 2018) which were not measured.

Aortic SMCs play an integral role in regulating wall contractility as well as matrix deposition and organization through force-dependent processes. In line with our results, standard histology reveals strong decays in SMC density between P21 and P98 (Murtada et al., 2020) and from P70 to P365 and then P730 aortas (Hemmeryckx et al., 2013). Our findings extend prior knowledge on SMCs by showing that both density and circumferential alignment of SMCs decrease continuously up to one year of age. The number of endothelial cells per intimal area, often difficult to determine in histology and left unquantified, also showed a strong decline during maturation while stabilizing after P98. It is well known that endothelial cells undergo major changes with age, including changes in shape and appearance during maturation and aging in rats though no reduction in cell number was reported (Haudenschild et al., 1981). Endothelial dysfunction in aging is a key contributor to compromised homeostasis (Sepúlveda et al., 2017), and aging seems to associate with increased sensitivity of endothelial cells to apoptotic stimuli (Hoffmann et al., 2001) and phenotypic and functional alterations associated with senescence (Bochenek et al., 2016). A more complex behavior was seen in adventitial cell density, with the strongest decline early on, confirming that the period P21-P42 is distinguished by rapid and unexpected microstructural changes.

In recent years, measuring changing arterial microstructure during mechanical testing has gradually gained in significance in the face of modeling challenges. In particular, adventitial collagen fibers of the aorta have been characterized during biaxial loading in terms of waviness (Chow et al., 2014), orientation (Haskett et al., 2012, 2013; Wan and Gleason, 2013; Chow et al., 2014; Cavinato et al., 2017, 2020; Krasny et al., 2018; Sherifova et al., 2019), fractal analysis (Chow et al., 2014), and volume fraction (Haskett et al., 2012). For elastic lamellae, most focus has been on the straightening, unfolding, and stretching of single elastic lamellae, leading to quantification of the waviness gradient through the aortic wall (Yu et al., 2018). In contrast, few studies have focused on 3D imaging of intramural cells (Wan et al., 2010; Spronck et al., 2016). To our knowledge, this is the first study of changing matrix and cell structure as a function of biaxial loading and aging. In addition, our regional analysis of the microstructure of dorsal and ventral sides of the descending thoracic aorta shed light on some differences that had not been emphasized before, which could be relevant to heterogeneous disease progression. In particular, we observed significant regional differences in collagen orientation and undulation. Moreover, an asymmetry in layer-specific thickness was found in these two regions and was consistent across ages and loading conditions.

Connecting microstructural parameters with biomechanical characteristics is a fundamental aspect of this study. It has been reported that the global axial stretch ratio and physiological circumferential elastic modulus increase in mouse thoracic aorta during the first postnatal month (Huang et al., 2006). Our group recently extended those findings in terms of both passive and active functions in conjunction with tissue composition in maturing descending

thoracic aorta up to P98 (Murtada et al., 2020). Fundamental metrics such as axial and circumferential stiffness and stored elastic energy increased after birth, reaching an asymptotic value by P56 that was considered a key point for biomechanical maturation. In aging, fully mature ascending thoracic aorta of $Eln^{+/+}$ wild-type mice show a reducing axial stretch from P180 to P730, though without clear changes in stiffness (inferred from pressure-volume relations, thus not comparable) despite increasing collagen and unchanged elastin (Hawes et al., 2020). In comparable samples of $Fbln5^{+/+}$ wild-type mice aged from P140 to P700, *in vivo* axial stretch declines with aging as do wall stress, material stiffness, and energy storage capability. These finding associated with increasing collagen area fraction and increases in collagen fiber width in the adventitia and media (Ferruzzi et al., 2018).

Introducing a continuity between postnatal maturation and aging, our study complements but extends prior studies via consistent analysis of sample-specific structure-function. In the interval P98-P140, not covered previously, there is a reversal of earlier changes in biaxial stress, stored energy, and axial stiffness, likely driven by an increased wall thickness and decreased axial stretch. The trend that leads to decreased circumferential stiffness reported by Ferruzzi and colleagues at two years seems not to occur up to one year. Importantly, in maturation and aging, axial material stiffness seems to be governed by the (primarily axially-oriented) fibrillar collagen fraction; on the other hand, circumferential stiffness associates with collagen morphology and alignment as well as SMC density and morphology, supporting prior suggestions about interactions between SMCs and ECM and ECM-driven SMC modulation which leads to pathologies in aged arteries (Sazonova et al., 2015). Interestingly, while EC density appeared to correlate with circumferential stiffness throughout aging, flow-mediated shear stress, which has been reported to elevate from P10-P21 and decrease to homeostatic values at P42 (Murtada et al., 2020), appeared to have a large influence on EC orientation. In addition, the significant increase in *in vivo* axial stretch between P21 and P42 correlated with a decrease in EC density, further emphasizing the significance of mechanical loading in the axial direction on EC properties and function. Moreover, the dramatic decrease in EC density between P21 and P98 is consistent with observations of reduced EC function around this stage reported by Murtada and colleagues. ECs are connected through adherens junction proteins such as VE-cadherins, and aging is known to increase the internalization and degradation of VE-cadherins (Chang et al., 2017). Thus, further investigation is needed to determine how mechanical loading and wall properties might affect cell-cell junctions during aging.

This study was limited in the sense that obtaining microstructural parameters for the primary aortic constituents from single imaging scans left other ECM components undetected. Notably, proteoglycans and matricellular proteins likely change with age and affect aortic mechanical properties. Similarly, information on the amount, location, and type of crosslinks in collagen fiber bundles was not collected though expected to affect structure-function relations, including possible non-affine to affine kinematic transformations under different loading conditions (Krasny et al., 2018; Cavinato et al., 2020). Hence, one must be careful not to overinterpret the correlation between stiffness and alignment of collagen bundles without information about the cross-links. As noted above, it has long been known that the SHG signal is weak in the media of murine arteries (Stoller et al., 2002; Wan et al., 2012; Cui et al., 2014), though the reason has remained unknown (Sugita and Matsumoto, 2017).

We reasoned, however, that the situation is similar for PSR-stained sections viewed under polarized light (Figure S4) – it is only by saturating the adventitial collagen signal that the medial collagen becomes visible in PSR, and now as we show SHG. Although one can focus on the medial collagen alone (Sugita and Matsumoto, 2017), the adventitia plays critical roles in central artery function (Gingras et al., 2009) thus we did not saturate its signal. We also did not focus solely on medial collagen since its primarily circumferential orientation renders its biomechanical contribution largely indistinguishable from that of the passive smooth muscle cells in bulk materials testing (Bellini et al., 2014). We note, however, that just as medial collagen can exhibit an axial orientation within the innermost media (Timmins et al., 2010), axially oriented fibers appear near the medial-adventitial border, apparently consistent with a prior report in the mouse aorta (Watson et al., 2016). This possible heterogeneous splay with sharp transitions within the media merits further investigation, particularly as it may change with disease states. Finally, the aorta exhibits different mechanical and histological properties along the vascular tree (Bersi et al., 2017), though we focused on the descending thoracic segment.

5. Conclusions

Postnatal maturation of the aorta involves diverse mechanobiological processes that define the homeostatic conditions that may be impacted by disease, with natural aging a primary risk factor for myriad sequelae. This study delineates the influence of age, at five stages from weaning to one year of natural aging, on aortic microstructural features under *in vivo* equivalent loading configurations, defined by age-specific blood pressures and sample-specific axial stretches, including the two primary extracellular matrix components and cells of the dorsal and ventral regions of the descending thoracic aorta. Effects of age on the 3D aortic microstructure were consistent with those on the passive mechanical and morphological metrics stemming from sample-specific biaxial testing. Correlations highlight relationships between the microstructural organization of collagen (layer-specific volume fraction, bundle and fiber dimensions, and orientation) and intramural cells (type-specific density and orientation) and the passive biomechanical metrics in both circumferential and axial directions. The present data show how advances of imaging, in addition to classical histology, can help understand better the microstructure and mechanics of the aging aorta, providing critical comparators for future studies of diverse diseases that may have different ages of onset.

Supplementary Material

Refer to Web version on PubMed Central for supplementary material.

Acknowledgments

This work was supported by grants from the US National Institutes of Health (R01 HL105297, U01 HL142518).

6. References

Baeyens N, Bandyopadhyay C, Coon BG, Yun S, Schwartz MA (2016). Endothelial fluid shear stress sensing in vascular health and disease. J. Clin. Invest 126, 821–828. doi:10.1172/JCI83083. [PubMed: 26928035]

Bellini C, Ferruzzi J, Roccabianca S, Di Martino ES, Humphrey JD (2014). A microstructurally motivated model of arterial wall mechanics with mechanobiological implications. Ann. Biomed. Eng 42, 488–502. doi:10.1007/s10439-013-0928-x. [PubMed: 24197802]

Bersi MR, Bellini C, Di Achille P, Humphrey JD, Genovese K, Avril S (2016). Novel methodology for characterizing regional variations in the material properties of murine aortas. J. Biomech. Eng 138. doi:10.1115/1.4033674.

Bersi MR, Khosravi R, Wujciak AJ, Harrison DG, Humphrey JD (2017). Differential cell-matrix mechanoadaptations and inflammation drive regional propensities to aortic fibrosis, aneurysm or dissection in hypertension. J. R. Soc. Interface 14. doi:10.1098/rsif.2017.0327.

Bochenek ML, Schütz E, Schäfer K (2016). Endothelial cell senescence and thrombosis: Ageing clots. Thromb. Res 147, 36–45. doi:10.1016/j.thromres.2016.09.019. [PubMed: 27669126]

Cavinato C, Badel P, Krasny W, Avril S, Morin C (2020). Experimental characterization of adventitial collagen fiber kinematics using Second-Harmonic Generation imaging microscopy: Similarities and differences across arteries, species and testing conditions, in Multi-scale Extracellular Matrix Mechanics and Mechanobiology, ed. Y. Zhang (Cham: Springer International Publishing), 123–164. doi:10.1007/978-3-030-20182-1_5.

Cavinato C, Helfenstein-Didier C, Olivier T, du Roscoat SR, Laroche N, Badel P (2017). Biaxial loading of arterial tissues with 3D in situ observations of adventitia fibrous microstructure: A method coupling multi-photon confocal microscopy and bulge inflation test. J. Mech. Behav. Biomed. Mater 74, 488–498. doi:10.1016/j.jmbbm.2017.07.022. [PubMed: 28751194]

Chang F, Flavahan S, Flavahan NA (2017). Impaired activity of adherens junctions contributes to endothelial dilator dysfunction in ageing rat arteries. J. Physiol 595, 5143–5158. doi:10.1113/JP274189. [PubMed: 28561330]

Chow M-J, Turcotte R, Lin CP, Zhang Y (2014). Arterial extracellular matrix: A mechanobiological study of the contributions and interactions of elastin and collagen. Biophys. J 106, 2684–2692. doi:10.1016/j.bpj.2014.05.014. [PubMed: 24940786]

Cui JZ, Tehrani AY, Jett KA, Bernatchez P, van Breeman C, Esfandiarei M (2014). Quantification of aortic and cutaneous elastin and collagen morphology in Marfan syndrome by multiphoton microscopy. Struct Biol. 187, 242–253. doi: 10.1016/j.jsb.2014.07.003

Disney CM, Lee PD, Hoyland JA, Sherratt MJ, Bay BK (2018). A review of techniques for visualising soft tissue microstructure deformation and quantifying strain Ex Vivo. J. Microsc doi:10.1111/jmi.12701.

Donato AJ, Walker AE, Magerko K, Bramwell RC, Black AD, Henson GD, et al. (2013). Life-long caloric restriction reduces oxidative stress and preserves nitric oxide bioavailability and function in arteries of old mice. Aging Cell 12, 772–783. doi:10.1111/acel.12103. [PubMed: 23714110]

Dutta S, Sengupta P (2016). Men and mice: Relating their ages. Life Sci. 152, 244–248. doi:10.1016/j.lfs.2015.10.025. [PubMed: 26596563]

Ferruzzi J, Bersi MR, Humphrey JD (2013). Biomechanical phenotyping of central arteries in health and disease: advantages of and methods for murine models. Ann. Biomed. Eng 41, 1311–1330. doi:10.1007/s10439-013-0799-1. [PubMed: 23549898]

Ferruzzi J, Madziva D, Caulk AW, Tellides G, Humphrey JD (2018). Compromised mechanical homeostasis in arterial aging and associated cardiovascular consequences. Biomech. Model. Mechanobiol 17, 1281–1295. doi:10.1007/s10237-018-1026-7. [PubMed: 29754316]

Fisher SA (2010). Vascular smooth muscle phenotypic diversity and function. Physiol. Genomics 42A, 169–187. doi:10.1152/physiolgenomics.00111.2010. [PubMed: 20736412]

Fleenor BS, Marshall KD, Durrant JR, Lesniewski LA, Seals DR (2010). Arterial stiffening with ageing is associated with transforming growth factor-β1-related changes in adventitial collagen: reversal by aerobic exercise. J. Physiol 588, 3971–3982. doi:10.1113/jphysiol.2010.194753. [PubMed: 20807791]

Flurkey K, Mcurrer J, Harrison D (2007). Mouse models in aging research, in The Mouse in Biomedical Research (Elsevier), 637–672. doi:10.1016/B978-012369454-6/50074-1.

Geifman N, and Rubin E (2013). The mouse age phenome knowledgebase and disease-specific interspecies age mapping. PLoS ONE 8. doi:10.1371/journal.pone.0081114.

Gingras M, Farand P, Safar ME, Plante GE (2009). Adventitia: the vital wall of conduit arteries. J. Am. Soc. Hypertens. JASH 3, 166–183. doi:10.1016/j.jash.2009.03.002. [PubMed: 20409958]

Gleason RL, Gray SP, Wilson E, Humphrey JD (2004). A multiaxial computer-controlled organ culture and biomechanical device for mouse carotid arteries. J. Biomech. Eng 126, 787–795. doi:10.1115/1.1824130. [PubMed: 15796337]

Goth W, Lesicko J, Sacks MS, Tunnell JW (2016). Optical-based analysis of soft tissue structures. Annu. Rev. Biomed. Eng 18, 357–385. doi:10.1146/annurev-bioeng-071114-040625. [PubMed: 27420574]

Greenwald SE (2007). Ageing of the conduit arteries. J. Pathol 211, 157–172. doi:10.1002/path.2101. [PubMed: 17200940]

Haskett D, Azhar M, Utzinger U, Vande Geest JP (2013). Progressive alterations in microstructural organization and biomechanical response in the ApoE mouse model of aneurysm. Biomatter 3, e24648. doi:10.4161/biom.24648. [PubMed: 23628871]

Haskett D, Speicher E, Fouts M, Larson D, Azhar M, Utzinger U, et al. (2012). The effects of angiotensin II on the coupled microstructural and biomechanical response of C57BL/6 mouse aorta. J. Biomech 45, 772–779. doi:10.1016/j.jbiomech.2011.11.017. [PubMed: 22196971]

Haudenschild CC, Prescott MF, Chobanian AV (1981). Aortic endothelial and subendothelial cells in experimental hypertension and aging. Hypertension 3. doi:10.1161/01.HYP.3.3_Pt_2.I148.

Hawes JZ, Cocciolone A, Cui AH, Griffin DB, Staiculescu MC, Mecham RP, et al. (2020). Elastin haploinsufficiency in mice has divergent effects on arterial remodeling with aging depending on sex. Am. J. Physiol.-Heart Circ. Physiol, ajpheart.00517.2020. doi:10.1152/ajpheart.00517.2020.

Helmchen F, Denk W (2005). Deep tissue two-photon microscopy. Nat. Methods 2, 932–940. doi:10.1038/nmeth818. [PubMed: 16299478]

Hemmeryckx B, Hoylaerts MF, Deloose E, Hove CEV, Fransen P, Bult H, et al. (2013). Age-associated pro-inflammatory adaptations of the mouse thoracic aorta. Thromb. Haemost 110, 785–794. doi:10.1160/TH13-01-0022. [PubMed: 23925372]

Hoffmann J, Haendeler J, Aicher A, Rössig L, Vasa M, Zeiher AM, et al. (2001). Aging enhances the sensitivity of endothelial cells toward apoptotic stimuli: important role of nitric oxide. Circ. Res 89, 709–715. doi:10.1161/hh2001.097796. [PubMed: 11597994]

Huang Y, Guo X, Kassab GS (2006). Axial nonuniformity of geometric and mechanical properties of mouse aorta is increased during postnatal growth. Am. J. Physiol.-Heart Circ. Physiol 290, H657–H664. doi:10.1152/ajpheart.00803.2005. [PubMed: 16172154]

Humphrey JD, Dufresne ER, Schwartz MA (2014). Mechanotransduction and extracellular matrix homeostasis. Nat. Rev. Mol. Cell Biol 15, 802–812. doi:10.1038/nrm3896. [PubMed: 25355505]

Humphrey JD, Tellides G (2019). Central artery stiffness and thoracic aortopathy. Am. J. Physiol.-Heart Circ. Physiol 316, H169–H182. doi:10.1152/ajpheart.00205.2018. [PubMed: 30412443]

Krasny W, Magoariec H, Morin C, Avril S (2018). Kinematics of collagen fibers in carotid arteries under tension-inflation loading. J. Mech. Behav. Biomed. Mater 77, 718–726. doi:10.1016/j.jmbbm.2017.08.014.. [PubMed: 28847434]

Le VP, Cheng JK, Kim J, Staiculescu MC, Ficker SW, Sheth SC, et al. (2015). Mechanical factors direct mouse aortic remodelling during early maturation. J. R. Soc. Interface 12, 20141350. doi:10.1098/rsif.2014.1350. [PubMed: 25652465]

Majesky MW (2015). Adventitia and perivascular cells. Arterioscler. Thromb. Vasc. Biol 35, e31–e35. doi:10.1161/ATVBAHA.115.306088. [PubMed: 26203160]

Murtada S-I, Kawamura Y, Li G, Schwartz MA, Tellides G, Humphrey JD (2020). Developmental origins of mechanical homeostasis in the aorta. Developmental Dynamics. doi:10.1002/dvdy.283.

Rezakhaniha R, Agianniotis A, Schrauwen JTC, Griffa A, Sage D, Bouten CVC, et al. (2012). Experimental investigation of collagen waviness and orientation in the arterial adventitia using confocal laser scanning microscopy. Biomech. Model. Mechanobiol 11, 461–473. doi:10.1007/s10237-011-0325-z. [PubMed: 21744269]

Roccabianca S, Figueroa CA, Tellides G, Humphrey JD (2014). Quantification of regional differences in aortic stiffness in the aging human. J. Mech. Behav. Biomed. Mater 29. doi:10.1016/j.jmbbm.2013.01.026.

Sazonova OV, Isenberg BC, Herrmann J, Lee KL, Purwada A, Valentine AD, et al. (2015). Extracellular matrix presentation modulates vascular smooth muscle cell mechanotransduction. Matrix Biol. 41, 36–43. doi:10.1016/j.matbio.2014.11.001. [PubMed: 25448408]

Schriefl AJ, Zeindlinger G, Pierce DM, Regitnig P, Holzapfel GA (2012). Determination of the layer-specific distributed collagen fibre orientations in human thoracic and abdominal aortas and common iliac arteries. J. R. Soc. Interface 9, 1275–1286. doi:10.1098/rsif.2011.0727. [PubMed: 22171063]

Schroeder F, Polzer S, Slazansky M, Man V, Skacel P (2018). Predictive capabilities of various constitutive models for arterial tissue. J. Mech. Behav. Biomed. Matl 78, 369–380. DOI: 10.1016/j.jmbbm.2017.11.035

Sepúlveda C, Palomo I, Fuentes E (2017). Mechanisms of endothelial dysfunction during aging: Predisposition to thrombosis. Mech. Ageing Dev 164, 91–99. doi:10.1016/j.mad.2017.04.011. [PubMed: 28477984]

Sherifova S, Sommer G, Viertler C, Regitnig P, Caranasos T, Smith MA, et al. (2019). Failure properties and microstructure of healthy and aneurysmatic human thoracic aortas subjected to uniaxial extension with a focus on the media. Acta Biomater. 99, 443–456. doi:10.1016/j.actbio.2019.08.038. [PubMed: 31465883]

Spronck B, Megens RTA, Reesink KD, Delhaas T (2016). A method for three-dimensional quantification of vascular smooth muscle orientation: application in viable murine carotid arteries. Biomech. Model. Mechanobiol 15, 419–432. doi:10.1007/s10237-015-0699-4. [PubMed: 26174758]

Stoller P, Celliers PM, Reiser KM, Rubenchik AM (2002). Imaging collagen orientation using polarization-modulated second harmonic generation. Proceed of SPIE. 4620, 157–165.

Sugita S, Matsumoto T (2017). Multiphoton microscopy observations of 3D elastin and collagen fiber microstructure changes during pressurization in aortic media. Biomech Model Mechanobiol. 16, 763–773. doi: 10.1007/s10237-016-0851-9 [PubMed: 27878400]

Timmins LH, Wu Q, Yeh AT, Moore JE, Greenwald SE (2010). Structural inhomogeneity and fiber orientation in the inner arterial media. Am J Physiol. 298, H1537–H1545. doi: 10.1152/ajpheart.00891.2009

Tsamis A, Phillippi JA, Koch RG, Pasta S, D'Amore A, Watkins SC, et al. (2013). Fiber micro-architecture in the longitudinal-radial and circumferential-radial planes of ascending thoracic aortic aneurysm media. J. Biomech 46, 2787–2794. doi:10.1016/j.jbiomech.2013.09.003. [PubMed: 24075403]

Turcotte R, Zhang Y (2020). Intrinsic optical imaging of ECM mechanics, in Multi-scale Extracellular Matrix Mechanics and Mechanobiology, ed. Y. Zhang (Cham: Springer International Publishing), 165–202. doi:10.1007/978-3-030-20182-1_6.

Wagenseil JE, Mecham RP (2009). Vascular extracellular matrix and arterial mechanics. Physiol. Rev 89, 957–989. doi:10.1152/physrev.00041.2008. [PubMed: 19584318]

Wan W, Gleason RL (2013). Dysfunction in elastic fiber formation in fibulin-5 null mice abrogates the evolution in mechanical response of carotid arteries during maturation. Am. J. Physiol.-Heart Circ. Physiol 304, H674–H686. doi:10.1152/ajpheart.00459.2012. [PubMed: 23241326]

Wan W, Dixon JB, Gleason RL (2012). Constitutive modeling of mouse carotid arteries using experimentally measured microstructural parameters. Biophys. J 102, 2916–2925. doi:10.1016/j.bpj.2012.04.035. [PubMed: 22735542]

Wan W, Yanagisawa H, Gleason RL (2010). Biomechanical and microstructural properties of common carotid arteries from fibulin-5 null mice. Ann. Biomed. Eng 38, 3605–3617. doi:10.1007/s10439-010-0114-3. [PubMed: 20614245]

Watson SR, Liu P, Peña EA, Sutton MA, Eberth JF, Lessner SM (2016). Comparison of aortic collagen fiber angle distribution in mouse models of atherosclerosis using second-harmonic generation (SHG) microscopy. Microsc. Microanal 22, 55–62. doi:10.1017/S1431927615015585. [PubMed: 26739629]

Wheeler JB, Mukherjee R, Stroud RE, Jones JA, Ikonomidis JS (2015). Relation of murine thoracic aortic structural and cellular changes with aging to passive and active mechanical properties. J. Am. Heart Assoc 4. doi:10.1161/JAHA.114.001744.

Yu X, Turcotte R, Seta F, Zhang Y (2018). Micromechanics of elastic lamellae: unravelling the role of structural inhomogeneity in multi-scale arterial mechanics. J. R. Soc. Interface 15, 20180492. doi:10.1098/rsif.2018.0492. [PubMed: 30333250]

Highlights

- Evolving thoracic aortic microstructure and mechanics were quantified and correlated over five ages, from weaning to one year of natural aging;
- Cell density reduced progressively in all three primary layers of the aorta and correlated with changes in passive mechanical metrics in the circumferential direction;
- Collagen fibers change dramatically during natural maturation and aging, dictating many tissue level metrics of mechanical functionality.

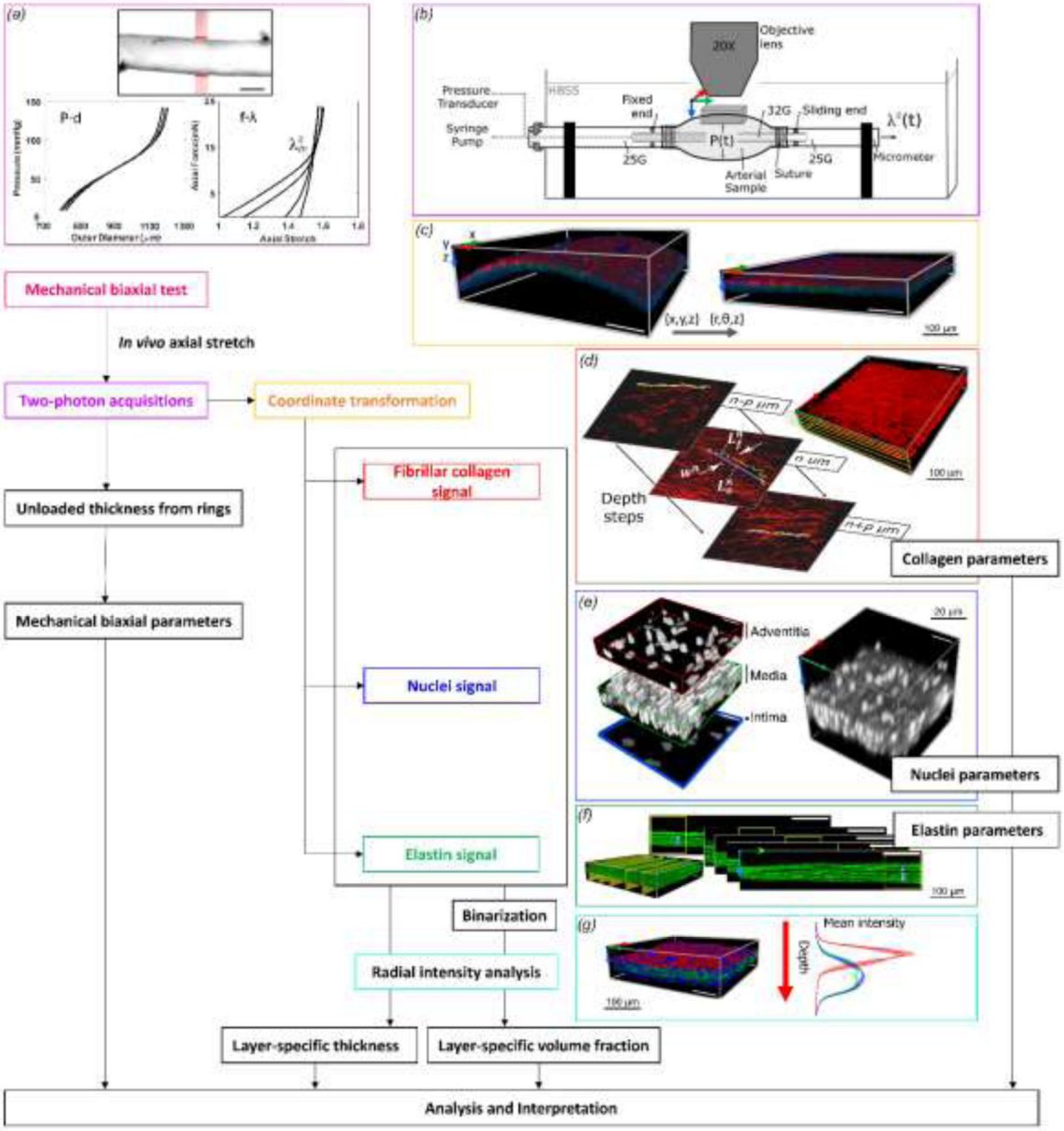

Figure 1. Schema of the workflow for mechanical testing, multiphoton imaging, and data analysis.

(a) A segment of the descending thoracic aorta was cannulated and phenotyped biomechanically under passive conditions using cyclic pressure - outer diameter (P–d) and axial force - axial stretch (f–λ) testing. Scale bar: 500 μm. (b) The sample was then re-canulated on a custom blunt-ended triple-needle assembly and mounted on a mechanical loading bench for multiphoton imaging, which allowed biaxial distension-extension as well as rigid body rotation around its axis. (c) A representative image showing a transformation from Cartesian-to-polar coordinates in 3D. Shown are the SHG signal of collagen (red), the auto-fluorescent signal of elastic lamellae (green), and the fluorescent signal of cell nuclei (blue). The color-coded coordinate system indicates circumferential (x, red), axial (y, green),

and radial (z, blue) directions. (d) In-plane straightness of collagen fibers and width w of the bundle containing the measured fiber were calculated for multiple fibers at prescribed radial positions across the wall. (e) Multiple volume subdomains from each 3D acquisition were used to estimate the number of cells per local volume of tissue with the images binarized before processing. Adventitial cell density and SMC density are reported as cell per 0.001 mm^3 of adventitia and media, respectively. Endothelial cell density refers to cells per 0.01 mm^2 of the inner-most surface. (*f*) *Number of elastic* lamellae *and interlamellar distance were measured in the circumferential-radial plane. (g)* L*ayer-specific analysis of thickness and volume fraction was performed using the mean intensity profiles of multiple volume subunits, before and after binarization, respectively*.

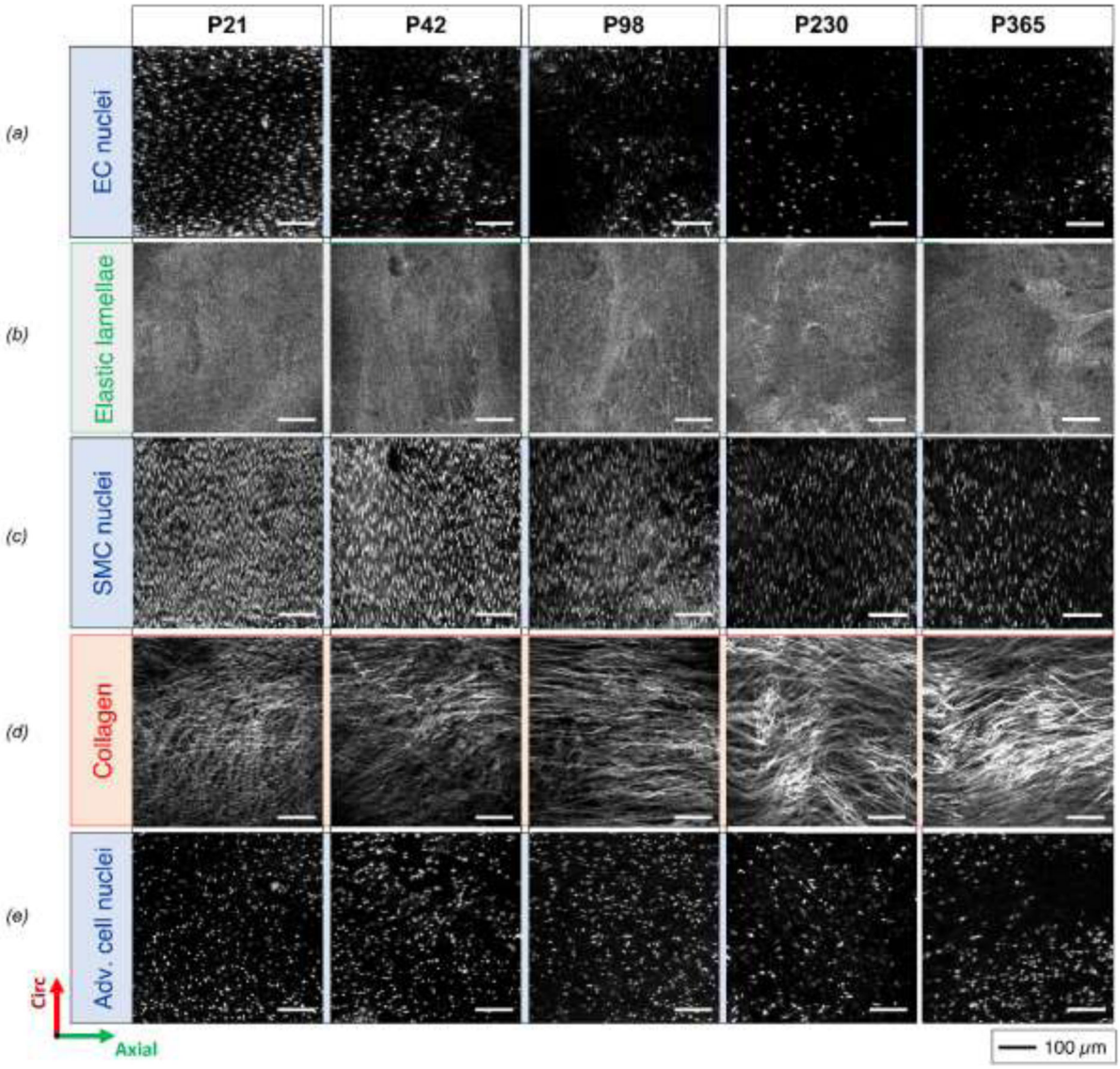

Figure 2.

Illustrative circumferential (vertical) – axial (horizontal) projections of 3D images of (top-to-bottom) EC nuclei, elastic lamellae, SMC nuclei, adventitial collagen, and adventitial cell nuclei for five ages (post-natal days P21, P42, P98, P230 and P365, ordered left-to-right in columns) at comparable configurations of ex vivo equivalent age-specific diastolic pressure and sample-specific in vivo axial stretch. For better visualization, the images of elastic lamellas are radial projections of the second elastic lamella from the lumen and not radial projections of the entire 3D image.

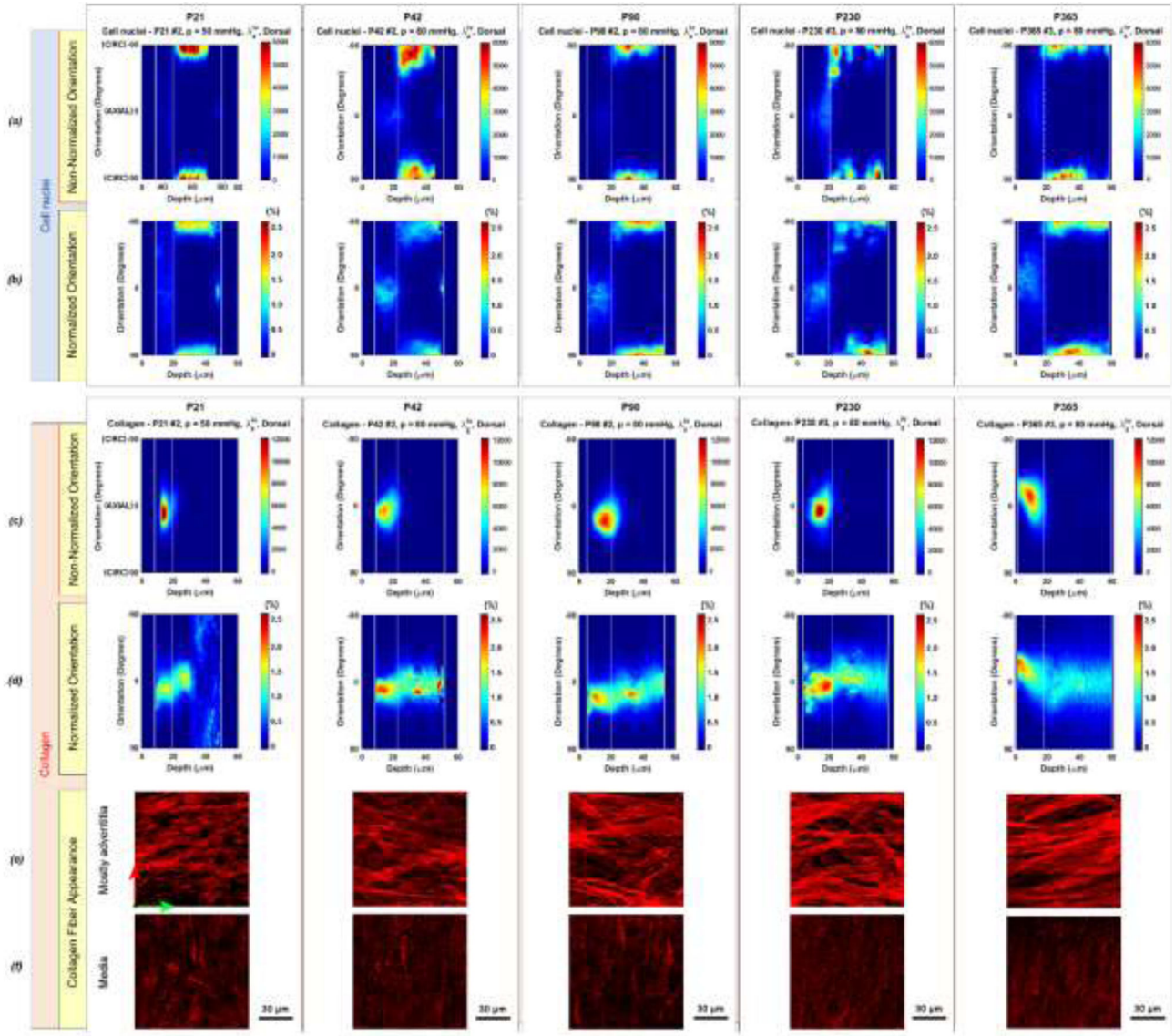

Figure 3.

Orientation of (a,b) cell nuclei (top box) and (c,d) collagen fibers (bottom box) as a function of radial position (depth) from the outer surface to the lumen for each age group (columns). The orientation varied between 0°, corresponding to the axial direction, and ±90°, corresponding to the circumferential direction. The white solid vertical lines indicate the outer (left) and inner (right) surface of the aortic wall and the white dotted line indicates the interface between the adventitial and medial layer. The raw orientation of (a) cell nuclei shows primarily the circumferential orientation of the SMC nuclei of the media whereas the raw orientation distribution of (c) collagen fibers shows primarily the axial component of adventitial fibers, varying slightly within samples. These raw intensity values are proportional to the number of pixels of the 3D image, with the gray levels categorized by orientation. When normalizing the distribution of nuclear orientations for each radial step separately by its area, one observes more clearly (b) a preferential axial component for adventitial nuclei and an axial component for endothelial cells of the inner surface in the P21

and P42 groups alone. Endothelial cells gradually lose this characteristic with aging and decrease in density. The normalized orientation distribution (d) of collagen shows an axial component in the outer medial layers, with P21 the only group characterized by a distinctive variation in collagen orientation along the radial direction toward a more circumferential orientation in the inner media. (e) Localized observations of collagen in the adventitia in small axial-circumferential regions (100μmx100 μm) confirmed the predominant axial orientation whereas (f) observations of collagen in the media, not including those near the medial-adventitial border, further revealed circumferential orientations only following a significant increase in contrast and brightness compared to (e); see also Figure S4. These findings demonstrate that the circumferential component captured in P21 samples arises from thin fibers that are circumferentially oriented and not organized into bundles. Fibers of similar appearance were also observed in older samples, however the limited presence of large bundles of collagen fibers, even in the medial layers, did not allow to capture the circumferential component of these thin fibers, much less bright than collagen bundles. The green and red arrows in the first column of (e) indicate axial and circumferential directions, respectively.

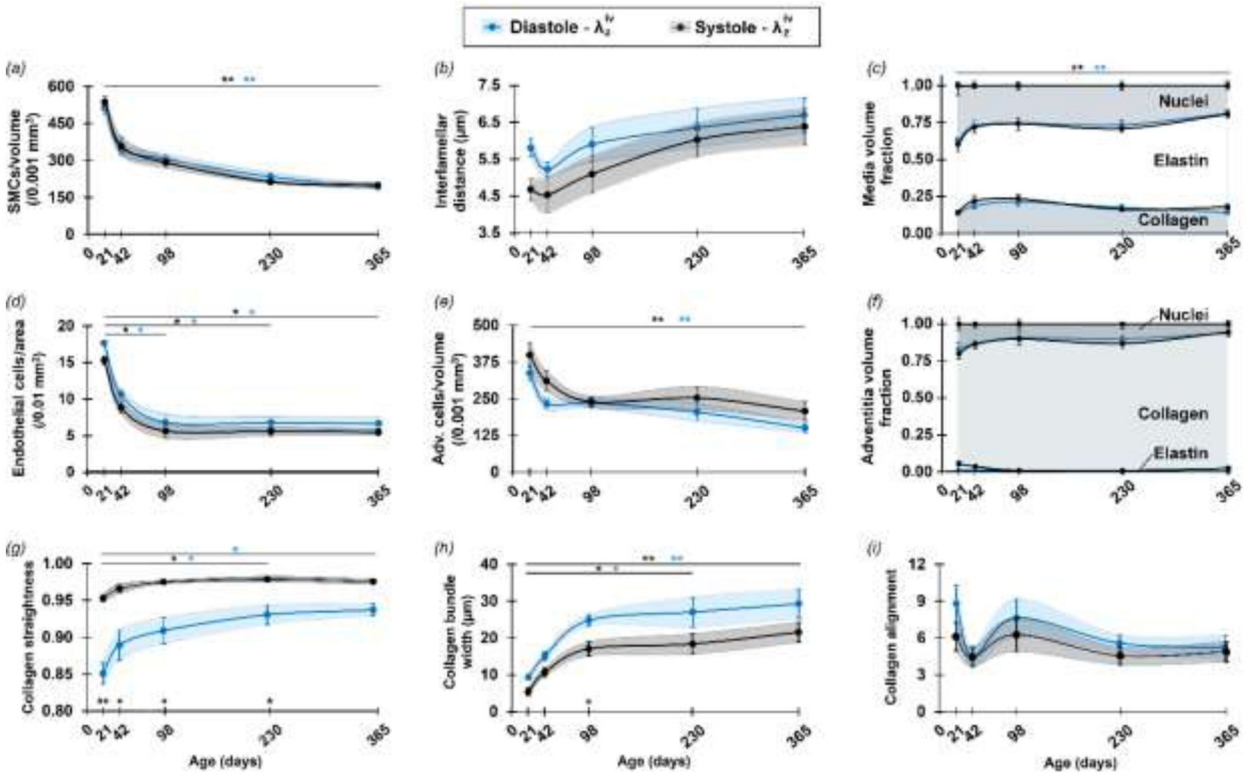

Figure 4.

Selected microstructural parameters for the DTA reveal distinct time courses of maturation and aging for postnatal days P21, P42, P98, P230 and P365. Values are evaluated at an ex vivo equivalent, age-specific diastolic (blue symbols) and systolic (black symbols) pressure and sample-specific in vivo axial stretch. Mean ± SEM (solid points and vertical bars) interconnected by smooth lines and SEM area (shadow area) indicate the progressive evolution of (a) SMC density, (b) elastin interlamellar distance, (d) endothelial cell density, (e) adventitial cell density, and (c, f) layer-specific (medial and adventitial) component volume fractions, (g) collagen straightness, (h) collagen bundle width, and (i) collagen alignment, the last three dominated by adventitial collagen. Overbars denote statistical significance between ages (the color identifies the pressure) and symbols over the x-axis denote statistical significance between pressures, where * $p<0.05$, ** $p<0.01$ and *** $p<0.001$. Note also that the total volume fraction (VF) value of 1 was the relative sum of fibrillar collagen, elastin, and nuclei and did not consider other components.

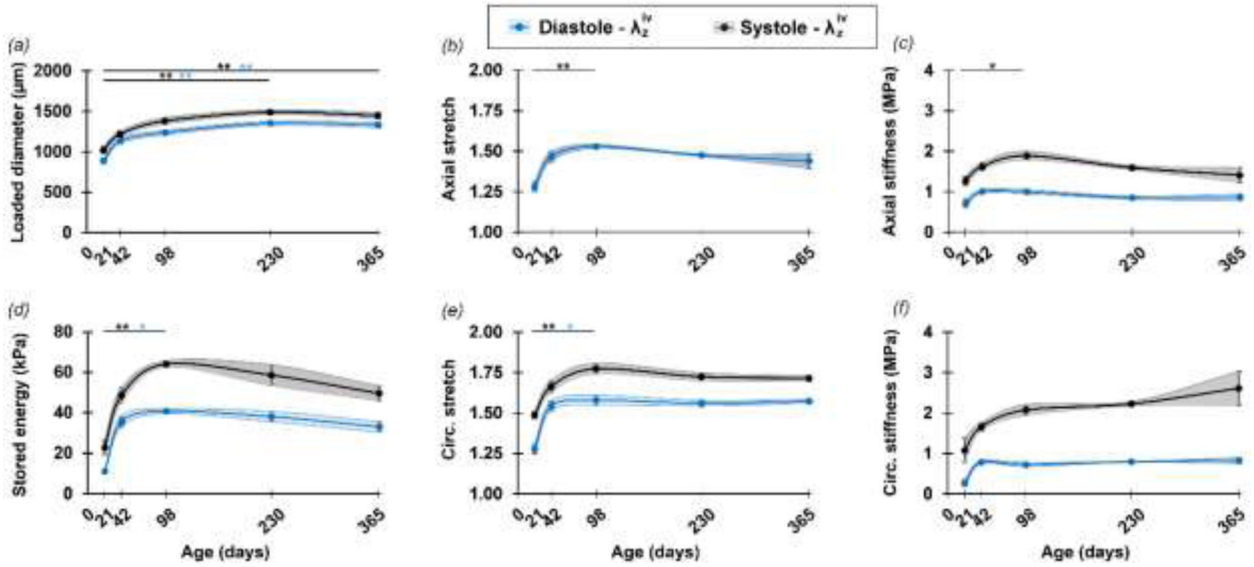

Figure 5.

Primary age-related differences in passive biomechanical metrics. Mean ± SEM values (solid points and vertical bars) interconnected by smooth lines and SEM area (shadow area) of (a) loaded diameter, (b) in vivo axial stretch, (c) axial stiffness (d) elastically stored energy, (e) circumferential stretch, and (f) circumferential stiffness, defined at age-specific ex-vivo equivalent diastolic (blue symbols) and systolic (black symbols) pressure for the DTA samples used for microstructural parameterization. Overbars denote statistical significance between ages (the color identifies the pressure), where * $p<0.05$, ** $p<0.01$ and *** $p<0.001$. A more detailed description of the passive mechanical function can be found in Figure S8.

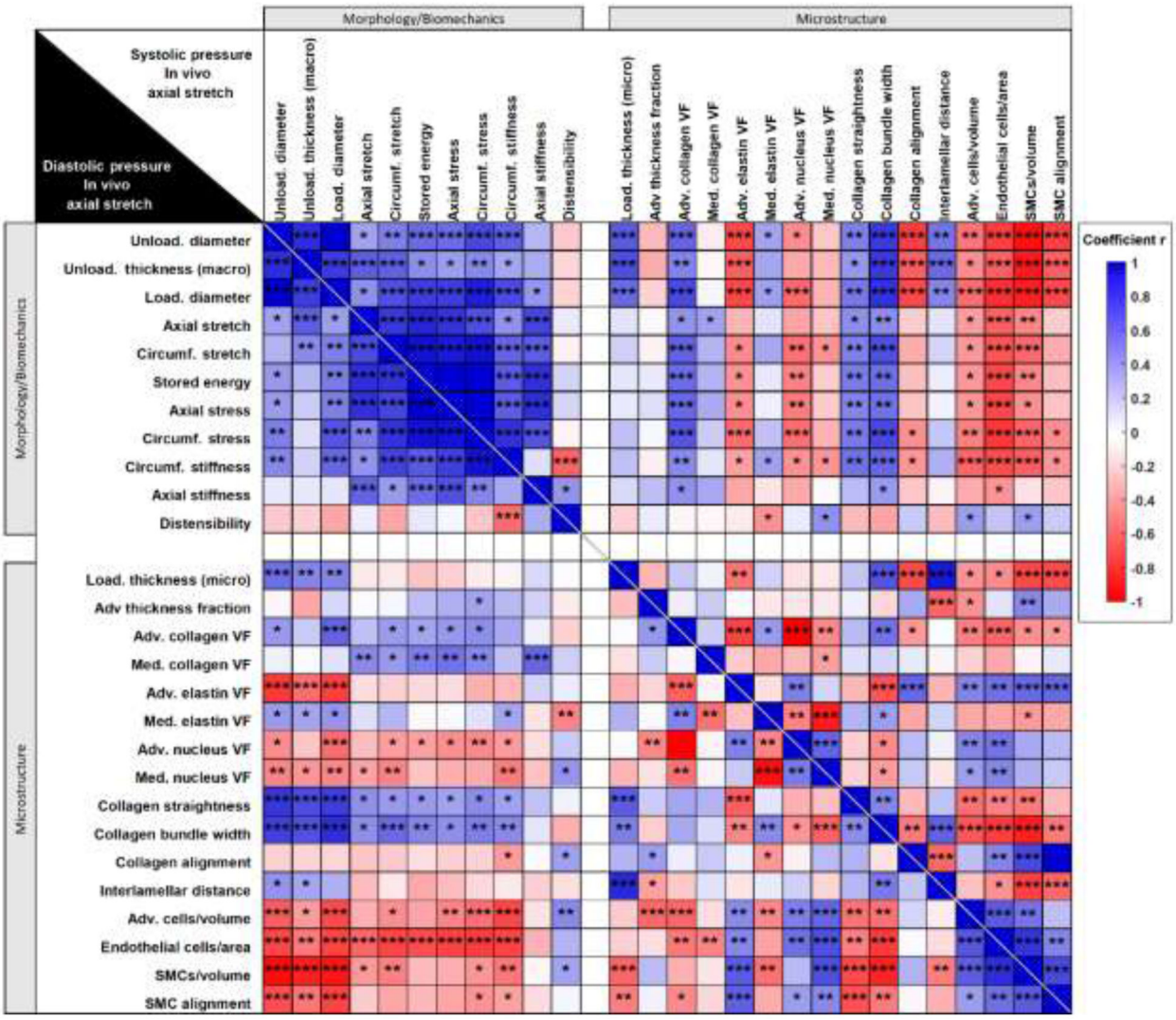

Figure 6.

Sample-specific macroscopic morphology, passive mechanical metrics, and microscopic parameters in statistical correlation for pooled age groups of DTA samples. All loaded metrics refer to the age-specific ex-vivo equivalent diastolic (lower left of the main diagonal) and systolic (upper right of the main diagonal) inner pressure and sample-specific in vivo axial stretch. Color scale map of the r coefficient with statistical significance symbols indicates statistical correlation among: (1) morphological parameters (diameter and thickness) measured or calculated from macroscopic observations, (2) primary passive biomechanical metrics, and (3) primary microscopic parameters quantified from two-photon images. Blue tiles indicate a positive correlation coefficient r and red tiles a negative correlation coefficient r. Statistical significance is represented by * $p<0.05$, ** $p<0.01$ and *** $p<0.001$. Unloaded thickness (macro) indicates the mean unloaded thickness of cross-sections of rings excised from each sample after the experiment whereas loaded thickness (micro) was measured from two-photon images at selected loading conditions as described

in Section 2.3. All coefficients and p-values are reported in Supplemental Materials Table S1 and Table S2.

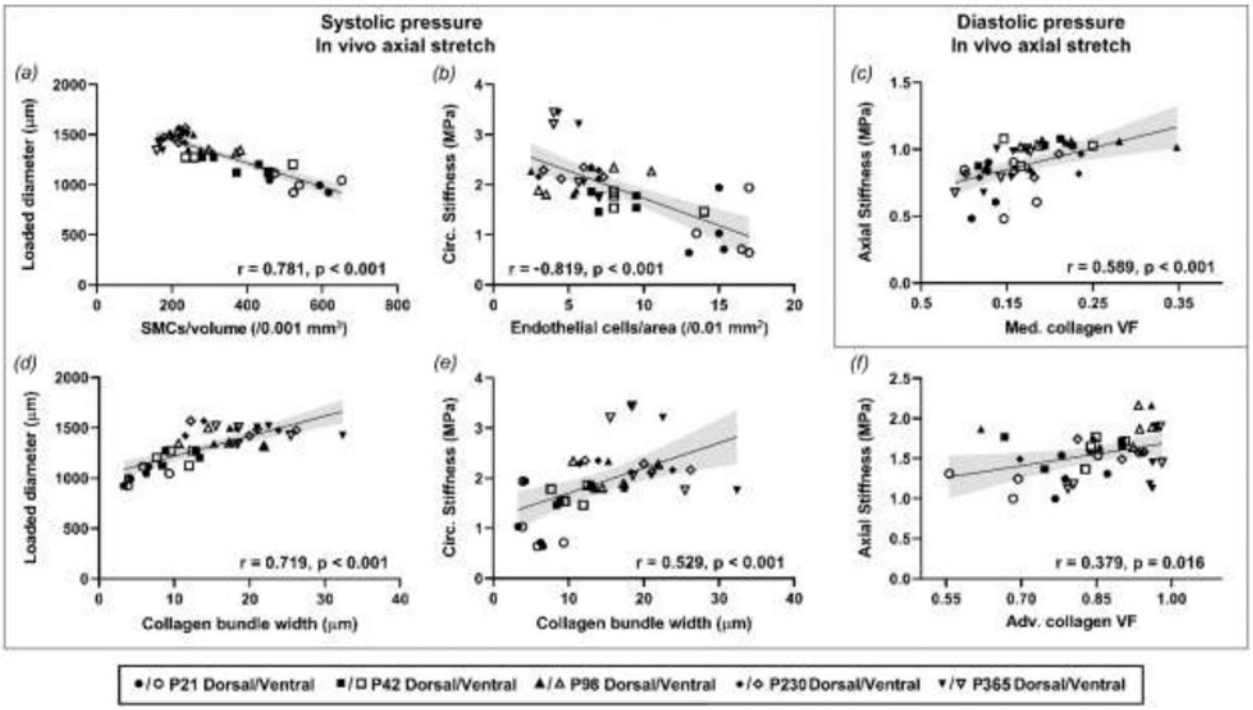

Figure 7.

Selected relationships showing significant correlations among passive mechanical, morphological, and microstructural parameters for pooled age groups of DTA samples. All metrics refer to the age-specific ex-vivo equivalent systolic (a-b, d-f) or diastolic (c) inner pressure and sample-specific in vivo axial stretch. Lines represent linear regressions, with 95%-confidence intervals shown with grey shading. Associated correlation coefficient r and p values are reported for each graph.